NEOPLASIA
www.neoplasia.com

Volume 20 Number 7 July 2018 pp. 734–744 734

DCE-MRI of Sunitinib-Induced Changes in Tumor Microvasculature and Hypoxia: A Study of Pancreatic Ductal Adenocarcinoma Xenografts[1,2]

Catherine S. Wegner, Anette Hauge, Trude G. Simonsen, Jon-Vidar Gaustad, Lise Mari K. Andersen and Einar K. Rofstad

Group of Radiation Biology and Tumor Physiology, Department of Radiation Biology, Institute for Cancer Research, Oslo University Hospital, Oslo, Norway

Abstract

The purpose of this study was dual: to investigate (a) whether sunitinib may induce changes in tumor microvasculature and hypoxia in pancreatic ductal adenocarcinoma (PDAC) and (b) whether any changes can be detected by DCE-MRI. Sunitinib-treated and untreated control tumors of two PDAC xenograft models (BxPC-3 and Panc-1) were subjected to DCE-MRI before the imaged tumors were prepared for quantitative analysis of immunohistochemical preparations. Pimonidazole was used as a hypoxia marker, and fraction of hypoxic tissue (HF_{Pim}), density of CD31-positive microvessels (MVD_{CD31}), and density of αSMA-positive microvessels ($MVD_{αSMA}$) were measured. Parametric images of K^{trans} and v_e were derived from the DCE-MRI data by using the Tofts pharmacokinetic model. BxPC-3 tumors showed increased HF_{Pim}, decreased MVD_{CD31}, unchanged $MVD_{αSMA}$, and increased vessel maturation index (VMI = $MVD_{αSMA}/MVD_{CD31}$) after sunitinib treatment. The increase in VMI was seen because sunitinib induced selective pruning rather than maturation of αSMA-negative microvessels. Even though the microvessels in sunitinib-treated tumors were less abnormal than those in untreated tumors, this microvessel normalization did not improve the function of the microvascular network or normalize the tumor microenvironment. In Panc-1 tumors, HF_{Pim}, MVD_{CD31}, $MVD_{αSMA}$, and VMI were unchanged after sunitinib treatment. Median K^{trans} increased with increasing MVD_{CD31} and decreased with increasing HF_{Pim}, and the correlations were similar for treated and untreated BXPC-3 and Panc-1 tumors. These observations suggest that sunitinib may induce significant changes in the microenvironment of PDACs, and furthermore, that K^{trans} may be an adequate measure of tumor vascular density and hypoxia in untreated as well as sunitinib-treated PDACs.

Neoplasia (2018) 20, 734–744

Introduction

In 1971, Judah Folkman proposed that antiangiogenesis would be important in the therapy of cancer [1], and in 1990, he provided significant evidence that tumor growth is angiogenesis dependent [2]. The pioneering work of Folkman created strong interest in tumor angiogenesis and antiangiogenic treatment of cancer, and today, antiangiogenic therapy is considered to be a promising cancer treatment modality [3]. Several molecular pathways promoting tumor angiogenesis have been identified, including the interleukin-8 (IL-8)/nuclear factor-κB (NF-κB) pathway, the angiopoietin (ANGPT)/tyrosine kinase with immunoglobulin-like and epidermal growth factor-like domains (TIE) pathway, and the vascular endothelial growth factor (VEGF)/VEGF receptor (VEGF-R) pathway [4,5]. The VEGF/VEGF-R pathway seems to be the most important

Abbreviations: αSMA, α smooth muscle actin; ANGPT/TIE, angiopoietin/tyrosine kinase with immunoglobulin-like and epidermal growth factor-like domains; DCE-MRI, dynamic contrast-enhanced magnetic resonance imaging; FOV, field of view; HE, hematoxylin and eosin; HF, hypoxic fraction; IL-8/NF-κB, interleukin-8/nuclear factor-κB; K^{trans}, volume transfer constant; MVD, microvessel density; PDAC, pancreatic ductal adenocarcinoma; ROI, region of interest; TE, echo time; TR, repetition time; v_e, fractional distribution volume; VEGF/VEGF-R, vascular endothelial growth factor/VEGF-receptor

Address all correspondence to: Einar K. Rofstad, PhD, Department of Radiation Biology, Institute for Cancer Research, Norwegian Radium Hospital, Box 4953 Nydalen, 0424 Oslo, Norway.
E-mail:; einar.k.rofstad@rr-research.no

[1] Funding: This work was supported by the Norwegian Cancer Society and the South-Eastern Norway Regional Health Authority.
[2] Conflict of Interest: The authors have no conflicts of interest.
Received 28 March 2018; Revised 16 May 2018; Accepted 21 May 2018

1476-5586/18
https://doi.org/10.1016/j.neo.2018.05.006

pathway, and many therapeutic drugs targeting this pathway have been developed, including the antibody bevacizumab and the tyrosine kinase inhibitors sorafenib and sunitinib [5,6]. A large number of clinical studies have been conducted, and it has been revealed that antiangiogenic therapy may not have a future as monotherapy, but used in combination with conventional chemotherapy or radiation therapy, antiangiogenic drugs may be important in the treatment of a large number of malignant diseases [5,7].

However, many factors limiting the effect of antiangiogenic drugs have been identified, one of which is the impact on the physicochemical microenvironment of tumors, particularly tumor oxygenation. This is a controversial issue, as some investigations suggest that antiangiogenic therapy may cause excessive vessel pruning leading to increased tumor hypoxia, whereas other investigations provide evidence that antiangiogenic therapy may lead to vessel normalization, increased perfusion, and improved tumor oxygenation [8,9]. Improved tumor oxygenation may decrease tumor aggressiveness and increase the effect of radiation therapy, immunotherapy, and some forms of chemotherapy, whereas elevated tumor hypoxia may impair the effects of most treatment modalities and promote tumor cell dissemination, invasion, and metastatic growth [10,11]. Importantly, it has been demonstrated that inhibition of the VEGF/VEGF-R pathway may increase the invasiveness and augment the metastatic potential of experimental tumors [12,13].

Noninvasive methods are needed to monitor the effect of antiangiogenic therapy on tumor oxygenation, and it has been suggested that physiological magnetic resonance imaging (MRI) may provide relevant parametric images [14–16]. This suggestion is supported by some preclinical studies that have compared the effect of antiangiogenic therapy on MRI-derived tumor parameters with that on tumor microenvironmental parameters assessed by invasive methods. Thus, it has been shown that multiparametric MRI, susceptibility contrast MRI, and MRI methods making use of ultrasmall superparamagnetic iron oxide particles as contrast agent may provide valid information on microvascular changes induced by antiangiogenic drugs [17–20]. However, similar studies examining the potential usefulness of established clinical MRI methods are sparse [21,22].

In our laboratory, studies of orthotopic A-07 melanoma xenografts – tumors that show a microenvironment characterized by highly permeable blood vessels and limited amounts of extracellular matrix components – have suggested that dynamic contrast-enhanced (DCE)-MRI is a potentially useful method for monitoring sunitinib-induced changes in tumor hypoxia [22]. This possibility was challenged in the study reported here by using pancreatic ductal adenocarcinoma (PDAC) xenografts as tumor models. The microenvironment of PDACs is characterized by an abundant desmoplastic stroma that may occupy large fractions of the tumor volume [23], and a dense extracellular matrix and poorly permeable blood vessels are important hallmarks of this stroma [24–26].

The purpose of this study was to investigate whether sunitinib can induce significant changes in the physicochemical microenvironment of PDAC xenografts, and furthermore, whether any changes can be detected by DCE-MRI. Tumors of two PDAC models (BxPC-3 and Panc-1) were included in the study. These models were selected because they differ substantially in tumor growth rate, differentiation, extracellular matrix distribution, angiogenic activity, microvascular density, and fraction of hypoxic tissue [27]. Sunitinib-induced changes in tumor microvasculature and hypoxia were assessed by quantitative analysis of histological preparations, and to investigate whether DCE-MRI is sensitive to sunitinib-induced changes, parametric images derived by pharmacokinetic analysis of DCE-MRI series were compared with the histological data.

Materials and Methods

Tumor Models

BxPC-3 and Panc-1 (American Type Culture Collection, VA, USA) human PDAC xenografts grown in adult (8–12 weeks of age) female BALB/c *nu/nu* mice were used as tumor models. Tumors were initiated from cells cultured in RPMI-1640 (25 mmol/l HEPES and L-glutamine) medium supplemented with 13% bovine calf serum, 250 mg/l penicillin, and 50 mg/l streptomycin. Approximately 2.5×10^6 cells in 25 µl of Hanks' balanced salt solution were inoculated intramuscularly in the left hind leg, and tumors were included in MRI experiments when having grown to a volume of 50–1200 mm^3.

Sunitinib Treatment

Sunitinib L-malate (LC Laboratories, Woburn, MA, USA) was dissolved in hydrochloric acid (1.0 molar ratio of sunitinib). Polysorbate 80 (0.5%; Sigma-Aldrich, Schnelldorf, Germany), polyethylene Glycol 300 (10%; Sigma Aldrich), sodium hydroxide to adjust to a pH of 3.5, and sterile water were added to the solution. Tumor-bearing mice were treated orally with sunitinib (40 mg/kg/day) or vehicle for 4 days.

Magnetic Resonance Imaging

MRI was carried out by using a Bruker Biospec 7.05-T bore magnet and a mouse quadrature volume coil (Bruker Biospin, Ettlingen, Germany). The tumors were positioned in the isocenter of the magnet and were imaged with axial slices covering the entire volume. The mice were given gas anesthesia (~4.0% Sevofluran in O_2; Baxter, IL, USA) at a flow rate of 0.5 l/min during imaging. Respiration rate and body core temperature were monitored continuously by using an abdominal pressure sensitive probe and a rectal temperature probe (Small Animal Instruments, New York, NY, USA). The body core temperature was kept at 37 °C by automated hot air flow regulation, and the gas anesthesia was adjusted manually to maintain a stable respiration rate.

DCE-MRI with Gd-DOTA (Dotarem, Guerbet, Paris, France) as contrast agent was performed as described earlier [27]. Anatomical T_2-weighted images were obtained prior to DCE-MRI by using a fast spin echo pulse sequence (RARE) with a repetition time (TR) of 2500 ms, an echo time (TE) of 35 ms, an image matrix of 128 × 128, a field of view (FOV) of 3 × 3 cm^2, a slice thickness of 0.7 mm, a slice gap of 0.3 mm, 2 averages, and fat suppression. A fast spin echo pulse sequence (RARE) with TRs of 200, 400, 800, 1500, 3000, and 5000 ms, TE of 8.5 ms, an image matrix of 128 × 128, a FOV of 3 × 3 cm^2, a slice thickness of 0.7 mm, and a slice gap of 0.3 mm was used to measure precontrast T_1-values (T_{10}-map). Gd-DOTA was diluted to a final concentration of 0.06 M and administered in the tail vein in a bolus dose of 5.0 ml/kg body weight during a period of 5 s by using an automated infusion pump (Harvard Apparatus, Holliston, MA, USA). A 3D SPGR pulse sequence (3D-FLASH) with a TR of 10 ms, a TE of 2.07 ms, a flip angle (α) of 20°, an image matrix of 128 × 128 × 10, and a FOV of 3 × 3 × 1 cm^3 was used to produce postcontrast T_1-weighted images at a temporal resolution of 14.8 s.

The analysis of the MRI data was based on the entire volume of the tumors. Regions of interest (ROIs) encompassing the tumor tissue were depicted in the T_2-weighted anatomical images, and these ROIs were transferred to the T_1-weighted images [27]. Numerical values of K^{trans} (the volume transfer constant of Gd-DOTA) and v_e (the fractional distribution volume of Gd-DOTA) were determined on a voxel-by-voxel basis by using the arterial input function reported by Benjaminsen et al. [28] and the Tofts pharmacokinetic model [29]. The pharmacokinetic analysis provided unphysiological v_e values ($v_e > 1.0$) for <10% of the voxels, and these voxels were excluded. It was verified that the tumors did not move during the imaging [27], and consequently, motion correction algorithms were not used.

Immunohistochemistry

Histological sections were prepared by standard procedures and stained with hematoxylin and eosin (HE) or immunostained for hypoxia, blood vessels, or pericytes, using a peroxidase-based immunohistochemical assay [30]. Pimonidazole [1-[(2-hydroxy-3-piperidinyl)-propyl]-2-nitroimidazole], injected as described earlier [30], was used as a marker of tumor hypoxia. CD31 and α-smooth muscle actin (αSMA) were used as markers of blood vessel endothelial cells and pericyte-covered blood vessels, respectively. An anti-pimonidazole rabbit polyclonal antibody (Professor James A. Raleigh, University of North Carolina, Chapel Hill, NC, USA), an anti-mouse CD31 rabbit polyclonal antibody (Abcam, Cambridge, UK), or an anti-mouse αSMA rabbit polyclonal antibody (Abcam) was used as primary antibody. Diaminobenzidine was used as chromogen, and hematoxylin was used for counterstaining. Quantitative studies were carried out on preparations cut through the central regions of tumors, and three sections of each staining were analyzed for each tumor. Microvessel density was scored by counting CD31-positive vessels (MVD_{CD31}) and αSMA-positive vessels ($MVD_{\alpha SMA}$) in whole tumor cross-sections [31]. Vessel maturation index (VMI) was calculated as VMI = $MVD_{\alpha SMA}/MVD_{CD31}$. Fraction of pimonidazole-positive tissue (*i.e.*, hypoxic fraction; HF_{Pim}) was assessed by image analysis [32] and was defined as the area fraction of the non-necrotic tissue showing positive staining.

Quantitative PCR

The RT^2 Profiler PCR Array Human Angiogenesis (PAHS-024Z; SABiosciences, Frederick, MD, USA) was used for expression profiling of angiogenesis-related genes. Total RNA was isolated from tumor tissue stabilized in RNA*later* RNA Stabilization Reagent (Qiagen, Hilden, Germany). RNA isolation, cDNA synthesis, and real-time PCR were carried out as described earlier [33]. Fold difference in gene expression was calculated by using the $\Delta\Delta C_T$-method [34]. A C_T-value of 35 (15 cycles above the positive PCR control) was set as detection limit. The arrays included 5 housekeeping genes [β-actin (ACTB), β-2-microglobulin (B2M), glyceraldehyde-3-phosphate dehydrogenase (GAPDH), hypoxanthine phosphoribosyltransferase 1 (HPRT1), ribosomal protein lateral stalk subunit P0 (RPLP0)], and each C_T-value of a tumor was normalized to the mean C_T-value of these genes as:

$$\Delta C_T = C_T^{\text{gene of interest}} - C_T^{\text{mean of housekeeping genes}}.$$

Normalized gene expression levels were calculated from three tumors as $2^{-\text{mean } \Delta CT}$.

Experimental Design

To investigate whether sunitinib may induce changes in tumor microvasculature and hypoxic fraction and whether any changes can be detected by DCE-MRI, tumors varying substantially in size were studied. Sunitinib treatment was given as described above, and the tumors were subjected to DCE-MRI one day after the last sunitinib dose. Pimonidazole was administered after the DCE-MRI when the mice had woken up and recovered from the anesthesia, and 3 to 4 hr. later, the tumors were resected and prepared for immunohistochemical examinations. Detailed studies with our anti-pimonidazole antibody have revealed that optimal discrimination between hypoxic and normoxic tumor tissue is achieved by allowing a time interval of 3 to 4 hr. between pimonidazole administration and tumor resection [35].

Statistical Analysis

The Pearson product moment correlation test was used to search for correlations between parameters. Curves were fitted to data by regression analysis. Comparisons of data were conducted by using the Student *t* test. The Kolmogorov–Smirnov method and the Levene's method were used to verify normality and equal variance, respectively. Probability values of $P < .05$, determined from two-sided tests, were considered significant. The statistical analysis was carried out with SigmaStat statistical software.

Results

Differences in Growth and Angiogenesis between BxPC-3 and Panc-1 Tumors

BxPC-3 tumors were differentiated and showed distinct ductal structures, whereas Panc-1 tumors were non-differentiated and showed an apparently random distribution of malignant cells (Supplementary Figure S1*A*). Growth rate measurements revealed that BxPC-3 tumors grew faster than Panc-1 tumors and, hence, had a shorter volume doubling time ($P < .0001$; Supplementary Figure S1*B*).

Adjacent histological preparations were stained for CD31 or αSMA to visualize blood vessels. The blood vessels were located in connective tissue rather than in parenchymal tissue, and this was particularly prominent in

Figure 1. Tumor angiogenesis. (A) Adjacent histological preparations stained for CD31 or αSMA to visualize blood vessels in a BxPC-3 and a Panc-1 tumor. Black arrows, examples of vessels showing positive staining for CD31, but not for αSMA. Red arrows, examples of vessels staining positive for both CD31 and αSMA. (B) Density of vessels staining positive for CD31 (MVD_{CD31}), density of vessels staining positive for αSMA ($MVD_{\alpha SMA}$), and vessel maturation index (VMI = $MVD_{\alpha SMA}/MVD_{CD31}$) for BxPC-3 and Panc-1 tumors. Columns and bars, mean ± SE of 20 tumors. (C) The expression of 84 angiogenesis-related genes in two BxPC-3 tumors plotted against each other and two Panc-1 tumors plotted against each other, illustrating that the expression did not differ significantly between single tumors of the same model. Points, single genes. Solid lines, 5-fold difference in expression between the two tumors compared in each panel. (D) The expression of 84 angiogenesis-related genes in BxPC-3 tumors compared with that in Panc-1 tumors. Points, mean values for single genes calculated from three BxPC-3 tumors and three Panc-1 tumors. Solid lines, 5-fold difference in expression between BxPC-3 and Panc-1 tumors. Red symbols, genes showing >5-fold higher expression in BxPC-3 tumors than in Panc-1 tumors. Green symbols, genes showing >5-fold higher expression in Panc-1 tumors than in BxPC-3 tumors. (E) The expression levels of the genes that showed >5-fold higher expression in Panc-1 tumors than in BxPC-3 tumors. (F) The expression levels of the genes that showed >5-fold higher expression in BxPC-3 tumors than in Panc-1 tumors. Columns and bars in (E) and (F), mean ± SE of three tumors.

BxPC-3 tumors. In both tumor models, only a low fraction of the CD31-positive vessels stained positive for αSMA (Figure 1*A*). Quantitative examinations revealed that MVD_{CD31} was higher in BxPC-3 tumors than in Panc-1 tumors ($P < .0001$), whereas Panc-1 tumors showed higher $MVD_{\alpha SMA}$ ($P < .0001$) and higher VMI ($P < .0001$) than BxPC-3 tumors (Figure 1*B*).

The differences in growth rate and MVD_{CD31} between BxPC-3 and Panc-1 tumors suggested that BxPC-3 tumors evoked higher angiogenic activity than Panc-1 tumors. The difference in angiogenic activity was studied further by measuring the expression levels of 84 angiogenesis-related genes, using a quantitative PCR assay. Three tumors of each model were examined, and significant differences between tumors of the same model

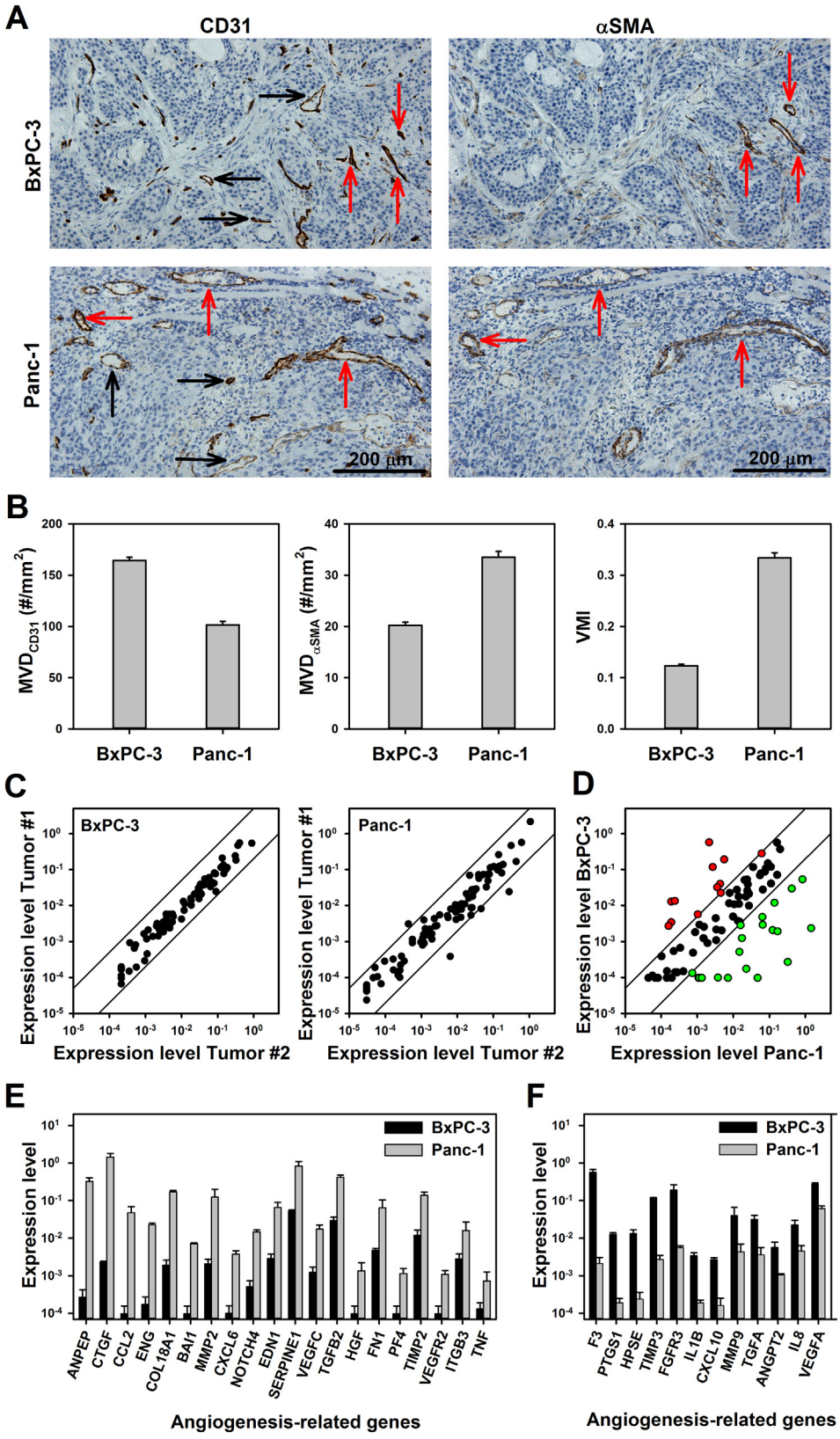

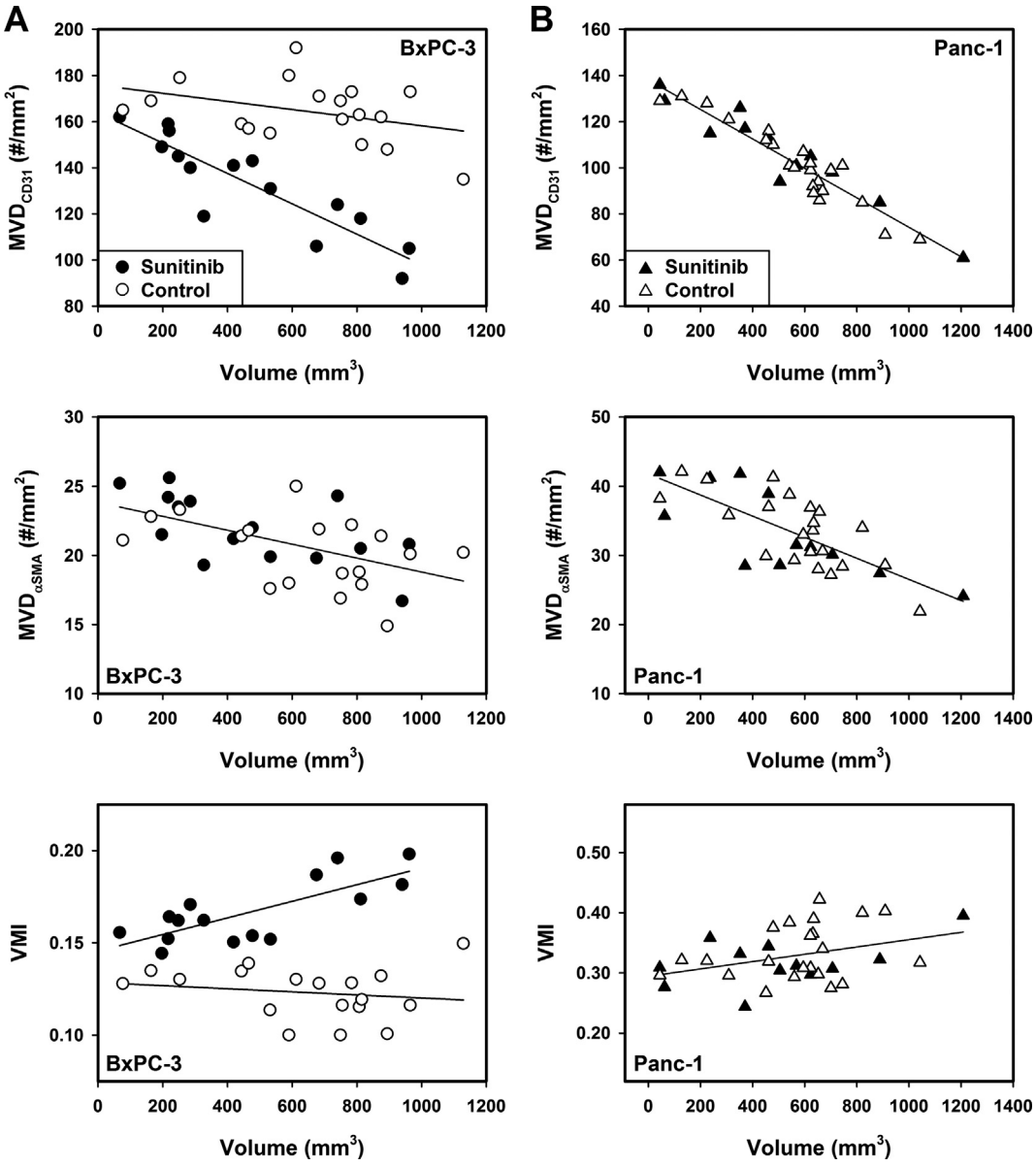

Figure 2. Tumor vascular density. Density of CD31-positive vessels (MVD_{CD31}), density of αSMA-positive vessels ($MVD_{αSMA}$), and vessel maturation index ($VMI = MVD_{αSMA}/MVD_{CD31}$) *versus* tumor volume for untreated and sunitinib-treated BxPC-3 (A) and Panc-1 (B) tumors. Points, single tumors. Curves, linear regression lines. A single curve was fitted to the data when the data for untreated and sunitinib-treated tumors were not significantly different.

could not be detected (Figure 1*C*). However, the expression levels differed substantially between the two models (Figure 1*D*). Twenty genes showed more than 5-fold higher expression in Panc-1 tumors than in BxPC-3 tumors (Figure 1*E*), whereas the expression level of 12 genes was more the 5-fold higher in BxPC-3 tumors than in Panc-1 tumors (Figure 1*F*). These 12 genes included VEGF-A, IL-8, and ANGPT2, suggesting that the elevated angiogenesis of BxPC-3 tumors was mediated by several pathways, including the VEGF/VEGF-R, IL-8/NFκB, and angiopoietin/TIE pathways. Because sunitinib binds to VEGF-R2, it is of interest to notice that Panc-1 tumors, in contrast to BxPC-3 tumors, showed significant VEGF-R2 expression (Figure 1*E*).

Sunitinib-Induced Changes in Tumor Microvasculature and Hypoxia

To investigate whether sunitinib induced changes in the microvasculature of BxPC-3 and Panc-1 tumors, histological sections of sunitinib-treated and untreated control tumors were immunostained for CD31 or αSMA and subjected to quantitative analysis. MVD_{CD31} and $MVD_{αSMA}$ decreased with increasing tumor volume in both models, regardless of whether the tumors were treated or not (Figure 2). Studies of BxPC-3 tumors showed that sunitinib induced a decrease in MVD_{CD31} ($P < .001$), whereas $MVD_{αSMA}$ was not changed after sunitinib treatment ($P > .05$). Consequently, VMI was higher in sunitinib-treated than in untreated tumors ($P < .001$, Figure 2*A*). In the Panc-1 model on the other hand, sunitinib-treated and untreated tumors did not differ in MVD_{CD31} ($P > .05$), $MVD_{αSMA}$ ($P > .05$), or VMI ($P > .05$), implying that sunitinib had no significant effect on the microvasculature of Panc-1 tumors (Figure 2*B*).

Sunitinib-induced changes in tumor hypoxia were studied by staining histological sections for the hypoxia marker pimonidazole. HF_{Pim} increased with increasing tumor volume in treated as well as

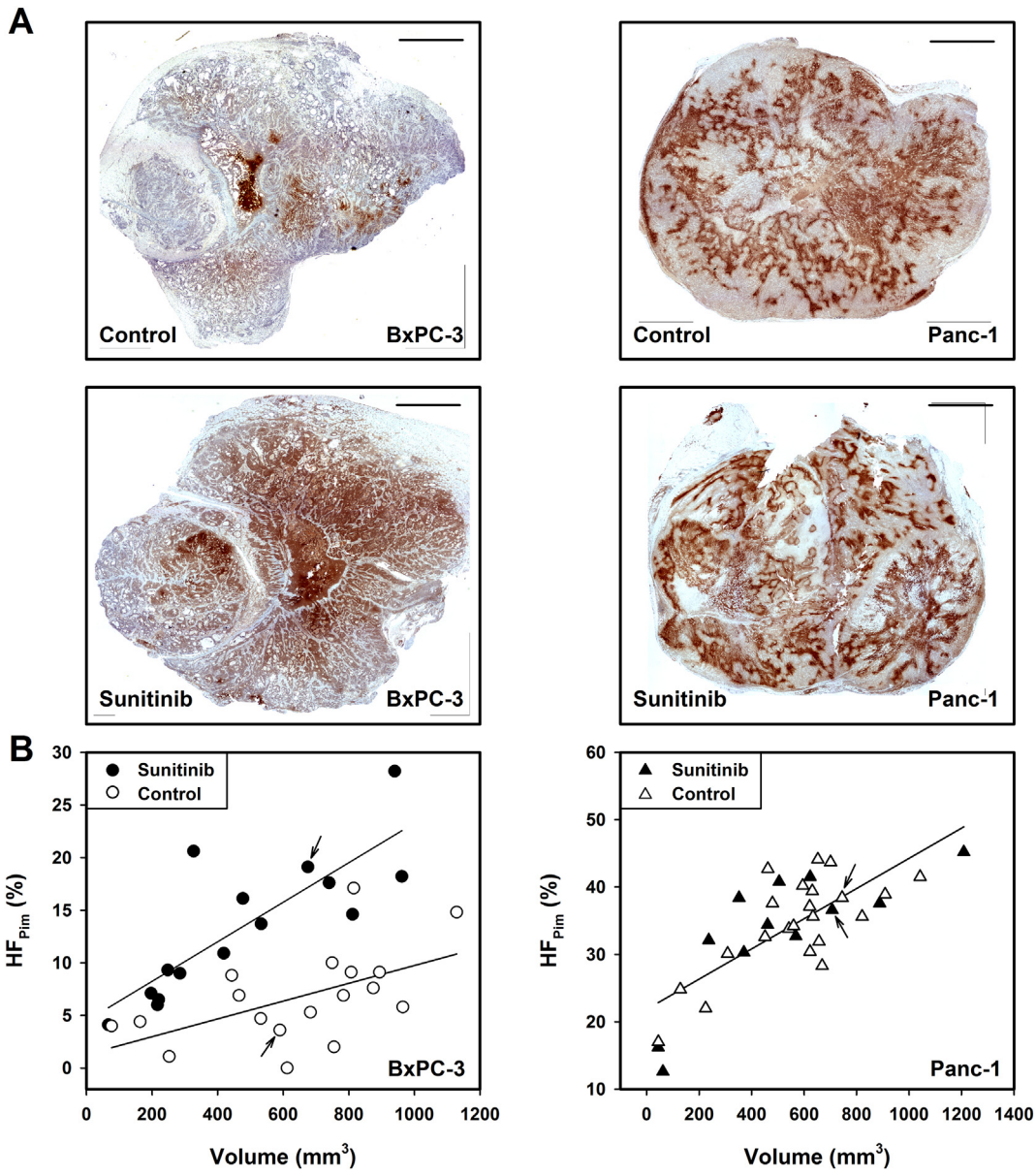

Figure 3. Tumor hypoxia. (A) Histological preparations stained for pimonidazole to visualize regions with hypoxic tissue in untreated and sunitinib-treated BxPC-3 and Panc-1 tumors. Scale bars, 2.0 mm. (B) Fraction of hypoxic tissue (HF_{Pim}) *versus* tumor volume for untreated and sunitinib-treated BxPC-3 and Panc-1 tumors. Points, single tumors. Curves, linear regression lines. The arrows identify the points referring to the tumors depicted in (A). A single curve was fitted to the Panc-1 data since the data for untreated and sunitinib-treated tumors were not significantly different.

untreated tumors (Figure 3). BxPC-3 tumors showed hypoxia staining mainly in central tumor regions, and these regions appeared to be larger in treated than in untreated tumors (Figure 3*A*), an observation that was confirmed by quantitative assessment of HF_{Pim} ($P < .005$, Figure 3*B*). In contrast, Panc-1 tumors showed foci of hypoxic tissue scattered throughout the entire tumor volume, and HF_{Pim} did not differ between treated and untreated tumors ($P > .05$, Figure 3, *A* and *B*).

Relationships between tumor hypoxia and microvasculature in sunitinib-treated and untreated tumors were studied by plotting MVD_{CD31} *versus* HF_{Pim} (Figure 4). As expected, MVD_{CD31} decreased with increasing HF_{Pim} in both tumor models, regardless of whether the tumors were treated or not. By comparing treated and untreated BxPC-3 tumors with the same MVD_{CD31}, it was revealed that the treated tumors had a lower HF_{Pim} than the untreated tumors ($P < .05$), suggesting that the blood and oxygen supply per microvessel had increased after sunitinib treatment. Significant differences between treated and untreated tumors could not be detected for the Panc-1 model ($P > .05$).

DCE-MRI of Sunitinib-Treated versus Untreated Control Tumors

The DCE-MRI data of the tumors were subjected to pharmacokinetic analysis using the Tofts model. Parametric images of K^{trans} and v_e and the corresponding K^{trans} and v_e frequency distributions of representative treated and untreated BxPC-3 and Panc-1 tumors are presented in Figure 5. The intratumor heterogeneity in K^{trans} and v_e was substantial in both tumor models. K^{trans} generally showed higher

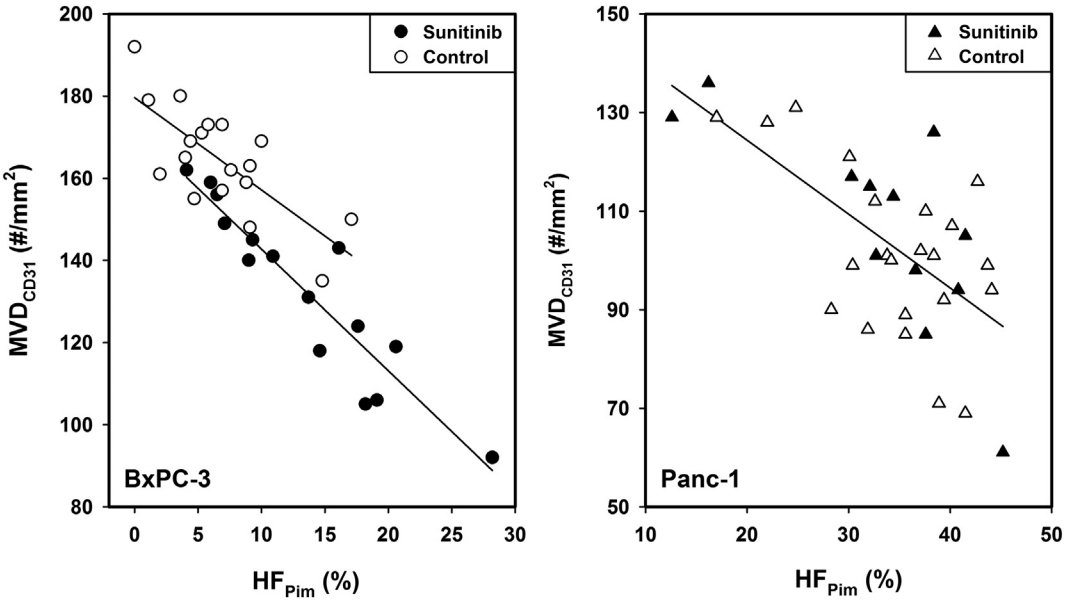

Figure 4. Tumor hypoxia and vascular density. Density of CD31-positive vessels (MVD_{CD31}) *versus* fraction of hypoxic tissue (HF_{Pim}) for untreated and sunitinib-treated BxPC-3 and Panc-1 tumors. Points, single tumors. Curves, linear regression lines. A single curve was fitted to the Panc-1 data since the data for untreated and sunitinib-treated tumors were not significantly different.

values in the tumor periphery than in central tumor regions, particularly in the BxPC-3 model, whereas high v_e values were seen both peripherally and centrally.

Quantitative analysis of the BxPC-3 tumors revealed that untreated tumors showed higher median K^{trans} than sunitinib-treated tumors ($P < .01$, Figure 6*A*), whereas median K^{trans} did not differ between treated and untreated Panc-1 tumors ($P > .05$, Figure 6*B*). Furthermore, median v_e did not differ between treated and untreated tumors in either of the models ($P > .05$; Figure 6, *A* and *B*). These observations are thus consistent with our hypothesis that low values of K^{trans} are associated with poor tumor vascularization and extensive tumor hypoxia [36–38].

This possibility was investigated further by plotting median K^{trans} *versus* MVD_{CD31} and HF_{Pim} (Figure 7). There was a strong positive correlation between median K^{trans} and MVD_{CD31} and a strong inverse correlation between median K^{trans} and HF_{Pim}, both for BxPC-3 tumors ($P < .0001$, Figure 7*A*) and Panc-1 tumors ($P < .0001$, Figure 7*B*). By comparing treated and untreated BxPC-3 tumors with the same MVD_{CD31}, it was seen that the treated tumors had a higher median K^{trans} than the untreated tumors ($P < .05$), suggesting that the blood supply per microvessel had increased after sunitinib treatment. A corresponding difference between treated and untreated tumors could not be detected for the Panc-1 model ($P > .05$). By comparing treated and untreated tumors having similar HF_{Pim}, it was revealed that median K^{trans} did not differ significantly between the two tumor groups in any of the models ($P > .05$). Furthermore, the relationships between median K^{trans} and MVD_{CD31} and between median K^{trans} and HF_{Pim} were similar for BxPC-3 and Panc-1 tumors, as illustrated by presenting the data for the two tumor models in the same plot (Figure 7*C*).

Discussion

This study used PDAC xenografts as preclinical tumor models and provides significant evidence that antiangiogenic treatment with sunitinib may induce changes in the microenvironment of tumors with an extensive stroma. The microenvironment of most experimental tumors becomes increasingly more hostile during tumor growth, with decreasing microvessel density and increasing fraction of hypoxic tissue [39]. It is therefore important to discriminate between treatment-induced and growth-induced microenvironmental changes in preclinical studies. If growth-induced changes are misinterpreted as treatment-induced changes, erroneous conclusions may be drawn. Our study was designed carefully to avoid this potential pitfall. Thus, tumors varying in size were studied, microenvironmental parameters were plotted *versus* tumor volume, and the regression curves for treated and untreated tumors were compared.

Clinical studies involving several histological types of cancer have revealed that some tumors respond to sunitinib treatment whereas others do not, but the reasons for this heterogeneity have not been identified conclusively [4–7]. Our study showed that sunitinib induced significant changes in the microvasculature of BxPC-3 tumors, whereas the microvasculature of Panc-1 tumors was unchanged after treatment. BxPC-3 tumors evoked higher angiogenic activity, grew faster, and developed a more immature microvasculature than Panc-1 tumors. Angiogenesis was probably mediated by the VEGF/VEGF-R, IL-8/NFκB, and angiopoietin/TIE pathways in both tumor models, but the expression of VEGF-A, IL-8, and ANGPT2 were more than 5-fold higher in BxPC-3 tumors than in Panc-1 tumors. Moreover, in contrast to BxPC-3 tumors, Panc-1 tumors showed significant expression of VEGFR-R2, an important target for sunitinib.

Effects of sunitinib on the microvasculature of tumors may depend on the sunitinib dose per treatment, the time between each treatment, and the number of treatments [7,40]. A relatively short treatment period of 4 days with daily sunitinib doses of 40 mg/kg was used in our study. It is possible that a longer treatment period or a higher sunitinib dose per treatment is required to induce microvascular changes in Panc-1 tumors.

Some investigators have provided evidence that antiangiogenic treatments targeting the VEGF/VEGF-R pathway may induce

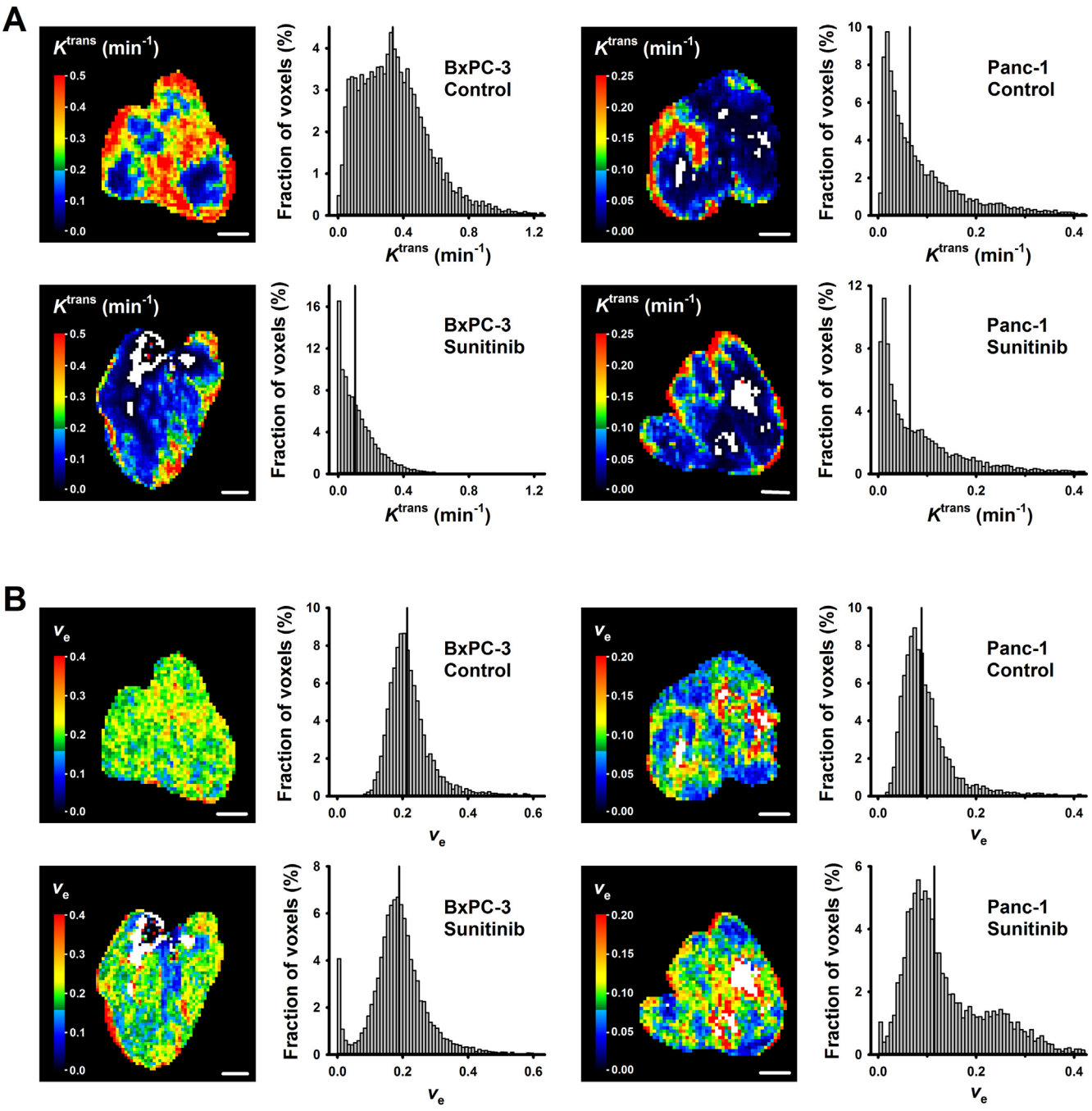

Figure 5. DCE-MRI-derived parametric images. Representative K^{trans} (A) and v_e (B) images and frequency distributions of an untreated BxPC-3 tumor, a sunitinib-treated BxPC-3 tumor, an untreated Panc-1 tumor, and a sunitinib-treated Panc-1 tumor. A central axial tumor section is shown in the parametric images, while individual voxel values from all tumor sections are included in the frequency distributions. Voxels with unphysiological v_e values (*i.e.*, $v_e > 1.0$) were excluded and appear white in the parametric images. Vertical lines in the frequency distributions, median values. Color bars, K^{trans} or v_e scales. Scale bars, 2.0 mm.

microvessel normalization in tumors and thus have suggested that also the tumor microenvironment may be normalized [40,41]. In the BxPC-3 model, VMI was higher in sunitinib-treated than in untreated tumors, and the supply of oxygen per microvessel was elevated after sunitinib treatment. The microvessels of sunitinib-treated tumors were thus less abnormal than those of untreated tumors. However, this microvessel normalization did not lead to normalization of the tumor microenvironment. Sunitinib-treated tumors showed decreased MVD_{CD31}, unchanged $MVD_{\alpha SMA}$, and increased HF_{Pim}, implying that sunitinib induced selective pruning rather than increased pericyte coverage of αSMA-negative microvessels. Due to the decreased MVD_{CD31}, the function of the microvascular network was impaired after sunitinib treatment, leading to a more hypoxic and hostile tumor microenvironment rather than microenvironmental normalization.

It has been claimed that antiangiogenic treatment-induced normalization of the microvasculature and microenvironment of tumors requires treatment doses that are sufficiently low to avoid

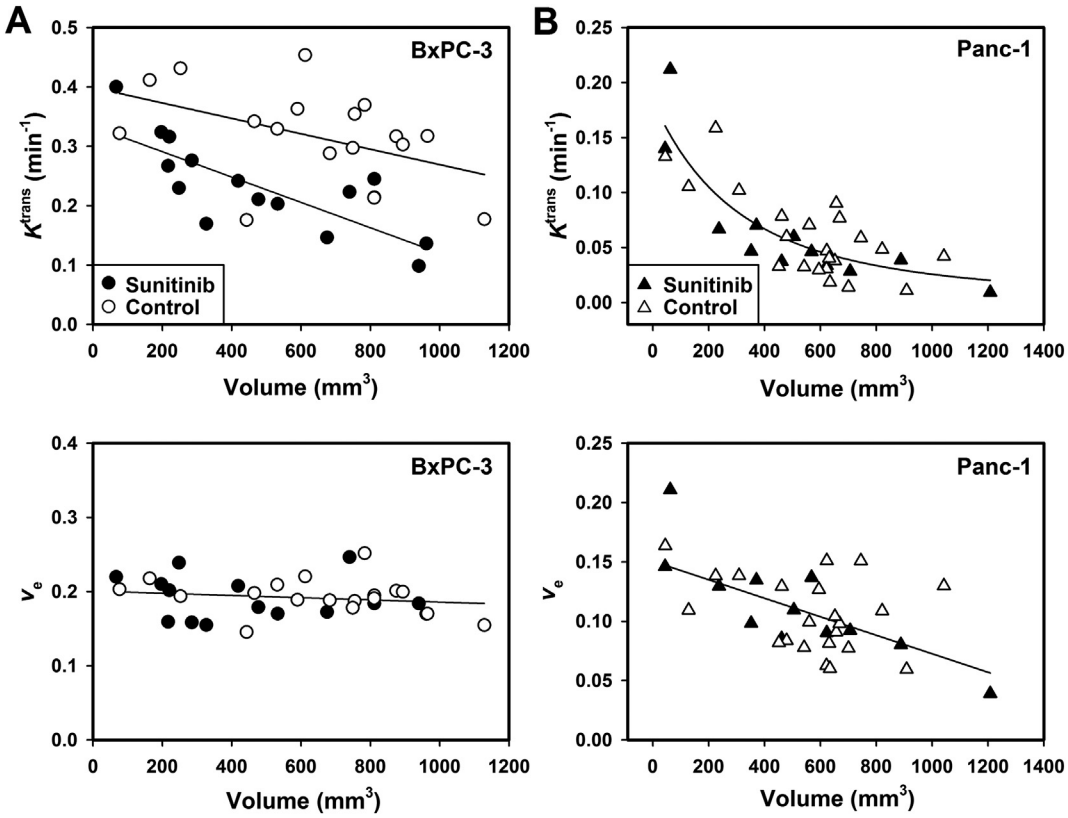

Figure 6. K^{trans} and v_e. Median K^{trans} and median v_e *versus* tumor volume for untreated and sunitinib-treated BxPC-3 (A) and Panc-1 (B) tumors. Points, single tumors. Curves, linear or exponential regression lines. A single curve was fitted to the data when the data for untreated and sunitinib-treated tumors were not significantly different.

microvessel pruning [40]. Panc-1 tumors were given sunitinib treatment according to the same protocol as BxPC-3 tumors, and even though a large fraction of the microvessels in Panc-1 tumors were immature and lacked pericyte coverage, the treatment did not cause microvessel pruning. VMI, MVD_{CD31}, and $MVD_{\alpha SMA}$ were similar in sunitinib-treated and untreated tumors, and furthermore, HF_{Pim} was not reduced in sunitinib-treated tumors, implying that sunitinib did not induce normalization of the microenvironment in Panc-1 tumors either.

There is significant evidence from preclinical studies that DCE-MRI may be a useful imaging modality for characterizing the physiological microenvironment of untreated tumors [21,38,42], and the possibility that DCE-MRI may be useful also for monitoring changes in the tumor microenvironment induced by antiangiogenic treatment was investigated in this study. Preclinical studies have significant advantages to clinical investigations because the imaging conditions can be controlled more easily. In the study reported here, the physiology of the imaged mice was monitored carefully, ensuring that tumor blood perfusion was not perturbed during image acquisition. After image acquisition, it was verified that the tumors had not moved during the imaging, thus allowing reliable voxelwise parametric images to be calculated from the DCE-MRI series. The DCE-MRI series were analyzed by using the Tofts pharmacokinetic model, and as illustrated elsewhere, this model gives good curve fits to single voxel data of BxPC-3 and Panc-1 tumors acquired with our DCE-MRI protocol [27].

The pharmacokinetic analysis provided parametric images of K^{trans} and v_e. According to the Tofts model, v_e is a measure of the distribution volume of the contrast agent, whereas K^{trans} is determined by the blood perfusion and the vessel permeability – vessel surface area product of the imaged tumor tissue [29]. In previous studies, we have shown that median K^{trans} is associated with the density of the microvascular network and the fraction of hypoxic tissue in untreated tumors [36–38]. The present study provided data suggesting that median K^{trans} is also sensitive to changes in tumor microvasculature and hypoxia induced by sunitinib treatment. In the BxPC-3 model, median K^{trans} was significantly lower in sunitinib-treated tumors than in untreated tumors, mirroring that sunitinib induced microvessel pruning and, hence, a decrease in MVD_{CD31} and an increase in HF_{Pim}. At the same MVD_{CD31}, median K^{trans} was higher in sunitinib-treated tumors than in untreated tumors, reflecting that the blood supply per microvessel was elevated after sunitinib treatment. In the Panc-1 model, on the other hand, median K^{trans} did not differ significantly between sunitinib-treated and untreated tumors, in accordance with the observation that sunitinib did not cause significant changes in MVD_{CD31} or HF_{Pim}.

Moreover, the associations between median K^{trans} and MVD_{CD31} or HF_{Pim} were similar for sunitinib-treated and untreated tumors in both models. By plotting the data for BxPC-3 and Panc-1 tumors together, it was seen that the data were well fitted by single curves, implying that similar relationships may exist for tumors differing clearly in biological characteristics and histological appearance. Consequently, DCE-MRI may have the potential to monitor changes in the microenvironment of tumors induced during sunitinib treatment.

It should be noticed that our study was conducted by using intramuscular rather than orthotopic PDAC xenografts as preclinical

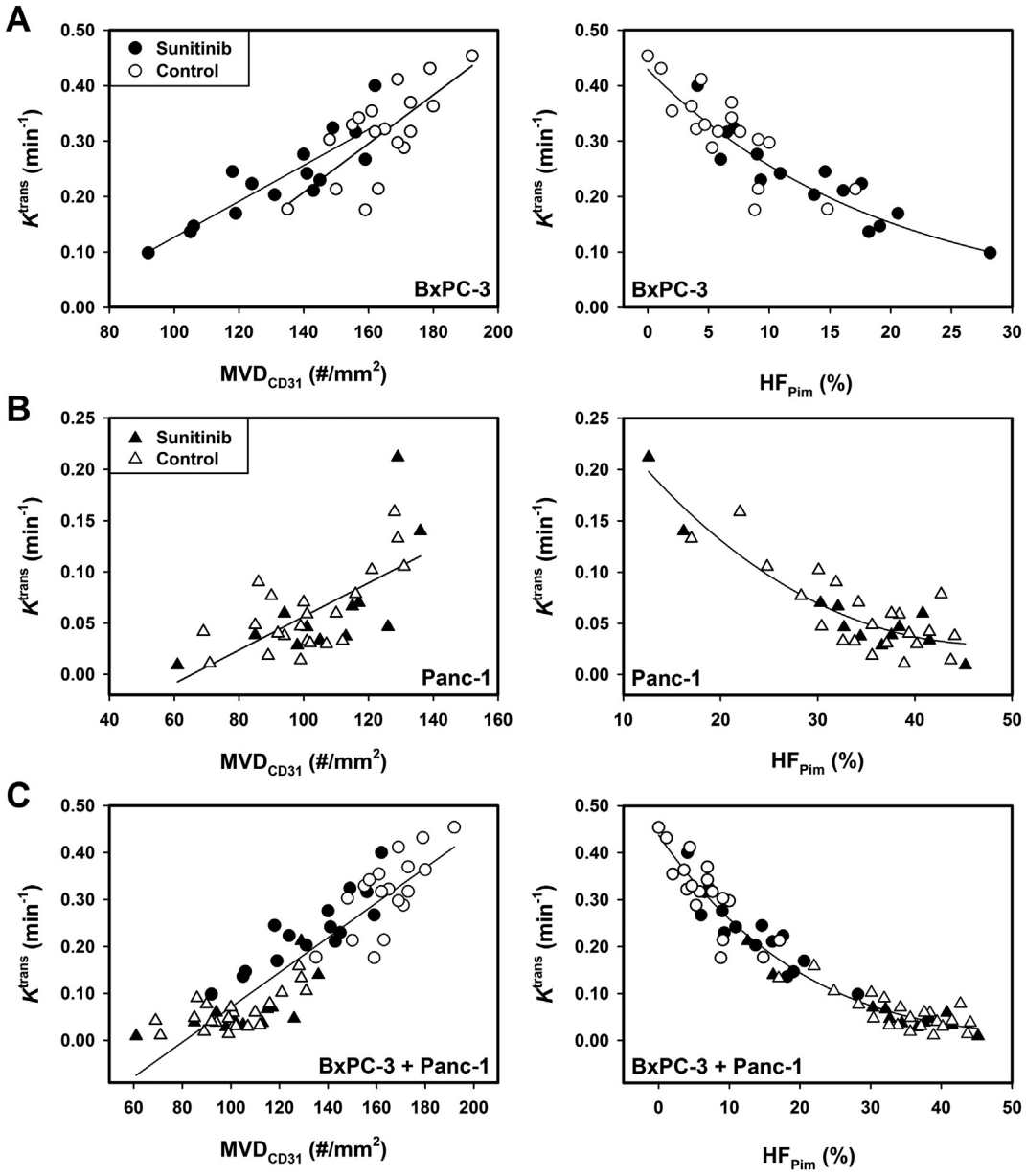

Figure 7. K^{trans}, tumor vascular density, and tumor hypoxia. Median K^{trans} *versus* density of CD31-positive vessels (MVD_{CD31}) and fraction of hypoxic tissue (HF_{Pim}) for untreated and sunitinib-treated BxPC-3 tumors (A), untreated and sunitinib-treated Panc-1 tumors (B), and untreated and sunitinib-treated BxPC-3 and Panc-1 tumors plotted together (C). Points, single tumors. Curves, linear or exponential regression lines. A single curve was fitted to the data when the data for untreated and sunitinib-treated tumors were not significantly different.

models of human PDAC. This is a limitation of the study because experimental PDACs transplanted to an ectopic site may not mirror the biology of human PDACs to the same extent as PDACs transplanted to the pancreas of mice [43,44]. However, an intramuscular site was chosen to avoid tumor movement due to respiration during the DCE-MRI. We have shown previously that intramuscular BxPC-3 and Panc-1 tumors have several microenvironmental features in common with human PDACs, including a histological appearance characterized by a dense collagen-rich extracellular matrix [38,45]. Furthermore, the numerical values of fraction of hypoxic tissue, microvascular density, and interstitial fluid pressure of intramuscular BxPC-3 and Panc-1 tumors are similar to those reported for orthotopic and genetically engineered mouse models of PDAC as well as human PDACs [45].

In summary, sunitinib may induce changes in the physicochemical microenvironment of PDAC xenografts. The sensitivity to sunitinib differs between tumor models, depending on the biology of the models. Median K^{trans} is associated with microvascular density and fraction of hypoxic tissue in sunitinib-treated and untreated tumors, and consequently, sunitinib-induced changes in the microenvironment in PDACs may be assessed by pharmacokinetic analysis of DCE-MRI recordings.

Supplementary data to this article can be found online at https://doi.org/10.1016/j.neo.2018.05.006.

Acknowledgments

We thank Kanthi Galappathi for valuable technical assistance. We carried out the DCE-MRI studies at the MRI Core Facility for Preclinical Cancer Research, Oslo University Hospital.

References

[1] Folkman J (1971). Tumor angiogenesis: therapeutic implications. *N Engl J Med* **285**, 1182–1186.

[2] Folkman J (1990). What is the evidence that tumors are angiogenesis dependent? *J Natl Cancer Inst* **82**, 4–6.

[3] Jayson GC, Kerbel R, Ellis LM, and Harris AL (2016). Antiangiogenic therapy in oncology: current status and future directions. *Lancet* **388**, 518–529.

[4] Gacche RN and Meshram RJ (2014). Angiogenic factors as potential drug target: efficacy and limitations of anti-angiogenic therapy. *Biochim Biophys Acta* **1846**, 161–179.

[5] Ebos JML and Kerbel RS (2011). Antiangiogenic therapy: impact on invasion, disease progression, and metastasis. *Nat Rev Clin Oncol* **8**, 210–221.

[6] Chen HX and Cleck JN (2009). Adverse effects of anticancer agents that target the VEGF pathway. *Nat Rev Clin Oncol* **6**, 465–477.

[7] Jayson GC, Hicklin DJ, and Ellis LM (2012). Antiangiogenic therapy—evolving view based on clinical trial results. *Nat Rev Clin Oncol* **9**, 297–303.

[8] De Bock K, Mazzone M, and Carmeliet P (2011). Antiangiogenic therapy, hypoxia, and metastasis: risky liaisons, or not? *Nat Rev Clin Oncol* **8**, 393–404.

[9] Cantelmo AR, Pircher A, Kalucka J, and Carmeliet P (2017). Vessel pruning or healing: endothelial metabolism as a novel target? *Expert Opin Ther Targets* **21**, 239–247.

[10] Bristow RG and Hill RP (2008). Hypoxia and metabolism. Hypoxia, DNA repair and genetic instability. *Nat Rev Cancer* **8**, 180–192.

[11] Wilson WR and Hay MP (2011). Targeting hypoxia in cancer therapy. *Nat Rev Cancer* **11**, 393–410.

[12] Pàez-Ribes M, Allen E, Hudock J, Takeda T, Okuyama H, Viñals F, Inoue M, Bergers G, Hanahan D, and Casanovas O (2009). Antiangiogenic therapy elicits malignant progesssion of tumors to increased local invasion and distant metastasis. *Cancer Cell* **15**, 220–231.

[13] Ebos JM, Lee CR, Cruz-Munoz W, Bjarnason GA, Christensen JG, and Kerbel RS (2009). Accelerated metastasis after short-term treatment with a potent inhibitor of tumor angiogenesis. *Cancer Cell* **15**, 232–239.

[14] O'Connor JPB and Jayson GC (2012). Do imaging biomarkers relate to outcome in patients treated with VEGF inhibitors? *Clin Cancer Res* **18**, 6588–6598.

[15] Zweifel M and Padhani AR (2010). Perfusion MRI in the early clinical development of antivascular drugs: decorations or decision making tools? *Eur J Nucl Med Mol Imaging* **37**(Suppl. 1), S164–S182.

[16] O'Connor JPB, Jackson A, Parker GJM, Roberts C, and Jayson GC (2012). Dynamic contrast-enhanced MRI in clinical trials of antivascular therapies. *Nat Rev Clin Oncol* **9**, 167–177.

[17] Boult JKR, Box G, Vinci M, Perryman L, Eccles SA, Jones C, and Robinson SP (2017). Evaluation of the response of intracranial xenografts to VEGF signaling inhibition using multiparametric MRI. *Neoplasia* **19**, 684–694.

[18] Robinson SP, Boult JKR, Vasudev NS, and Reynolds AR (2017). Monitoring the vascular response and resistance to sunitinib in renal cell carcinoma *in vivo* with susceptibility MRI. *Cancer Res* **77**, 4127–4134.

[19] Matsumoto S, Batra S, Saito K, Yasui H, Choudhuri R, Gadisetti C, Subramanian S, Devasahayam N, Munasinghe JP, and Mitchell JB, et al (2011). Antiangiogenic agent sunitinib transiently increases tumor oxygenation and suppresses cycling hypoxia. *Cancer Res* **71**, 6350–6359.

[20] Lemasson B, Christen T, Serduc R, Maisin C, Bouchet A, Le Duc G, Rémy C, and Barbier EL (2012). Evaluation of the relationship between MR estimates of blood oxygen saturation and hypoxia: effect of an antiangiogenic treatment on a gliosarcoma model. *Radiology* **265**, 743–752.

[21] Hillman GG, Singh-Gupta V, Zhang H, Al-Bashir AK, Katkuri Y, Li M, Yunker CK, Patel AD, Abrams J, and Haacke EM (2009). Dynamic contrast-enhanced magnetic resonance imaging of vascular changes induced by sunitinib in papillary renal cell carcinoma xenograft tumors. *Neoplasia* **11**, 910–920.

[22] Gaustad JV, Pozdniakova V, Hompland T, Simonsen TG, and Rofstad EK (2013). Magnetic resonance imaging identifies early effects of sunitinib treatment in human melanoma xenografts. *J Exp Clin Cancer Res* **32**, 93.

[23] Whatcott CJ, Diep CH, Jiang P, Watanabe A, LoBello J, Sima C, Hostetter G, Shepard HM, Von Hoff DD, and Han H (2015). Desmoplasia in primary tumors and metastatic lesions of pancreatic cancer. *Clin Cancer Res* **21**, 3561–3568.

[24] Feig C, Gopinathan A, Neesse A, Chan DS, Cook N, and Tuveson DA (2012). The pancreas cancer microenvironment. *Clin Cancer Res* **18**, 4266–4276.

[25] Bijlsma MF and van Laarhoven HWM (2015). The conflicting roles of tumor stroma in pancreatic cancer and their contribution to the failure of clinical trials: a systematic review and critical appraisal. *Cancer Metastasis Rev* **34**, 97–114.

[26] Grzesiak JJ, Ho JC, Moossa AR, and Bouvet M (2007). The integrin-extracellular matrix axis in pancreatic cancer. *Pancreas* **35**, 293–301.

[27] Wegner CS, Gaustad JV, Andersen LMK, Simonsen TG, and Rofstad EK (2016). Diffusion-weighted and dynamic contrast-enhanced MRI of pancreatic adenocarcinoma xenografts: associations with tumor differentiation and collagen content. *J Transl Med* **14**, 161.

[28] Benjaminsen IC, Graff BA, Brurberg KG, and Rofstad EK (2004). Assessment of tumor blood perfusion by high-resolution dynamic contrast-enhanced MRI: a preclinical study of human melanoma xenografts. *Magn Reson Med* **52**, 269–276.

[29] Tofts PS, Brix G, Buckley DL, Evelhoch JL, Henderson E, Knopp MV, Larsson HB, Lee TY, Mayr NA, and Parker GJ, et al (1999). Estimating kinetic parameters from dynamic contrast-enhanced T1-weighted MRI of a diffusable tracer: standardized quantities and symbols. *J Magn Reson Imaging* **10**, 223–232.

[30] Rofstad EK, Rasmussen H, Galappathi K, Mathiesen B, Nilsen K, and Graff BA (2002). Hypoxia promotes lymph node metastasis in human melanoma xenografts by up-regulating the urokinase-type plasminogen activator receptor. *Cancer Res* **62**, 1847–1853.

[31] Rofstad EK, Huang R, Galappathi K, Andersen LMK, Wegner CS, Hauge A, Gaustad JV, and Simonsen TG (2016). Functional intratumoral lymphatics in patient-derived xenograft models of squamous cell carcinoma of the uterine cervix: implications for lymph node metastasis. *Oncotarget* **7**, 56986–56997.

[32] Rofstad EK, Galappathi K, Mathiesen B, and Ruud EB (2007). Fluctuating and diffusion-limited hypoxia in hypoxia-induced metastasis. *Clin Cancer Res* **13**, 1971–1978.

[33] Simonsen TG, Gaustad JV, Leinaas MN, and Rofstad EK (2012). High interstitial fluid pressure is associated with tumor-line specific vascular abnormalities in human melanoma xenografts. *PLoS One* **7**e40006.

[34] Vanguilder HD, Vrana KE, and Freeman WM (2008). Twenty-five years of quantitative PCR for gene expression analysis. *Biotechniques* **44**, 619–626.

[35] Rofstad EK and Måseide K (1999). Radiobiological and immunohistochemical assessment of hypoxia in human melanoma xenografts: acute and chronic hypoxia in individual tumours. *Int J Radiat Biol* **75**, 1377–1393.

[36] Egeland TAM, Gulliksrud K, Gaustad JV, Mathiesen B, and Rofstad EK (2012). Dynamic contrast-enhanced-MRI of tumor hypoxia. *Magn Reson Med* **67**, 519–530.

[37] Ellingsen C, Hompland T, Galappathi K, Mathiesen B, and Rofstad EK (2014). DCE-MRI of the hypoxic fraction, radioresponsiveness, and metastatic propensity of cervical carcinoma xenografts. *Radiother Oncol* **110**, 335–341.

[38] Wegner CS, Hauge A, Gaustad JV, Andersen LMK, Simonsen TG, Galappathi K, and Rofstad EK (2017). Dynamic contrast-enhanced MRI of the microenvironment of pancreatic adenocarcinoma xenografts. *Acta Oncol* **56**, 1754–1762.

[39] Moulder JE, Dutreix J, Rockwell S, and Siemann DW (1988). Applicability of animal tumor data to cancer therapy in humans. *Int J Radiat Oncol Biol Phys* **14**, 913–927.

[40] Jain RK (2013). Normalizing tumor microenvironment to treat cancer: bench to bedside to biomarkers. *J Clin Oncol* **17**, 2205–2218.

[41] Martin JD, Fukumura D, Duda DG, Boucher Y, and Jain RK (2016). Reengineering the tumor microenvironment to alleviate hypoxia and overcome cancer heterogeneity. *Cold Spring Harb Perspect Med* **6**, a027094.

[42] Zhao D, Jiang L, Hahn EW, and Mason RP (2005). Continuous low-dose (metronomic) chemotherapy on rat prostate tumors evaluated using MRI in vivo and comparison with histology. *Neoplasia* **7**, 678–687.

[43] Kimbrough CW, Hudson S, Khanal A, Egger ME, and McNally LR (2015). Orthotopic pancreatic tumors detected by optoacoustic tomography using Syndecan-1. *J Surg Res* **193**, 246–254.

[44] Fleming JB and Brekken RA (2003). Functional imaging of angiogenesis in an orthotopic model of pancreatic cancer. *J Cell Biochem* **90**, 492–501.

[45] Andersen LMK, Wegner CS, Simonsen TG, Huang R, Gaustad JV, Hauge A, Galappathi K, and Rofstad EK (2017). Lymph node metastasis and the physicochemical microenvironment of pancreatic ductal adenocarcinoma xenografts. *Oncotarget* **8**, 48060–48074.